Monthly Notices
of the
ROYAL ASTRONOMICAL SOCIETY

MNRAS **464,** 1676–1692 (2017)
Advance Access publication 2016 October 5

doi:10.1093/mnras/stw2436

Revisiting CFHTLenS cosmic shear: optimal E/B mode decomposition using COSEBIs and compressed COSEBIs

Marika Asgari,[1]★ Catherine Heymans,[1] Chris Blake,[2] Joachim Harnois-Deraps,[3] Peter Schneider[4] and Ludovic Van Waerbeke[3]

[1]*Scottish Universities Physics Alliance, Institute for Astronomy, University of Edinburgh, Royal Observatory, Blackford Hill, Edinburgh EH9 3HJ, UK*
[2]*Centre for Astrophysics and Supercomputing, Swinburne University of Technology, P.O Box 218, Hawthorn, VIC 3122, Australia*
[3]*Department of Physics and Astronomy, University of British Columbia, 6224 Agricultural Road, Vancouver V7T 1Z1, B.C, Canada*
[4]*Argelander-Institut für Astronomie, Universität Bonn, Auf dem Hügel 71, D-53121 Bonn, Germany*

Accepted 2016 October 4. Received 2016 August 30; in original form 2015 December 21

ABSTRACT

We present a re-analysis of the CFHTLenS weak gravitational lensing survey using Complete Orthogonal Sets of E/B-mode Integrals, known as COSEBIs. COSEBIs provide a complete set of functions to efficiently separate E-modes from B-modes and hence allow for robust and stringent tests for systematic errors in the data. This analysis reveals significant B-modes on large angular scales that were not previously seen using the standard E/B decomposition analyses. We find that the significance of the B-modes is enhanced when the data are split by galaxy type and analysed in tomographic redshift bins. Adding tomographic bins to the analysis increases the number of COSEBIs modes, which results in a less-accurate estimation of the covariance matrix from a set of simulations. We therefore also present the first compressed COSEBIs analysis of survey data, where the COSEBIs modes are optimally combined based on their sensitivity to cosmological parameters. In this tomographic CCOSEBIs analysis, we find the B-modes to be consistent with zero when the full range of angular scales are considered.

Key words: gravitational lensing: weak – methods: data analysis – cosmology: observations – large-scale structure of Universe.

1 INTRODUCTION

Observations of weak gravitational lensing by the large-scale structure in the Universe provides a powerful probe of dark matter, dark energy and modified gravity theories. The underlying physics of lensing is well understood, leaving the non-trivial measurement itself as the main challenge in reaching the full potential of this cosmological tool. Three major new weak lensing surveys are under way, with the Kilo-Degree Survey (KiDS), the Dark Energy Survey (DES) and the Hyper-Suprime Camera Survey (HSC). KiDS and DES recently presented their first 'cosmic shear' measurements (Becker et al. 2016; Kuijken et al. 2015). These new surveys already cover several hundreds of square degrees; but for now they still lack statistical precision in comparison to their deeper but smaller area predecessor, the Canada–France–Hawaii Telescope Lensing Survey, CFHTLenS (Heymans et al. 2012). As such, this survey still provides the tightest cosmological constraints from weak gravitational lensing.

The tension between the results of the CFHTLenS tomographic analysis (Heymans et al. 2013) and the cosmological measurements from the cosmic microwave background (Planck Collaboration et al. 2016a) has been widely reported. It has been interpreted in different ways as a sign for new physics (see for example Battye & Moss 2014; Dossett et al. 2015; Planck Collaboration XIV 2016b), the combined effects of baryonic feedback and neutrinos (Harnois-Déraps et al. 2015; Köhlinger et al. 2016) or previously unknown systematic errors (see for example Verde et al. 2013; Addison et al. 2016; Raveri 2015; Spergel, Flauger & Hložek 2015). In this paper, we address the question of systematic errors by subjecting the CFHTLenS data to a rigorous test for shear systematics using "Complete Orthogonal Sets of E/B-mode Integrals" also known as "COSEBIs". Gravitational lensing can only produce E-modes and any detected B-modes are due to either systematic errors or other physical effects.[1]

The formalism for COSEBIs was developed in Schneider, Eifler & Krause (2010). COSEBIs provide a complete set of functions for efficiently separating E-modes from B-modes and hence allow for robust systematics tests using the B-modes and a fairly compressed data set. Schneider et al. (2010) and Eifler (2011) showed

★ E-mail: ma@roe.ac.uk

[1] Whereas source clustering and lens–lens coupling can in principle generate B-modes from lensing (Schneider, van Waerbeke & Mellier 2002; Hilbert et al. 2009), their amplitude is too small to be significantly detected in current and future surveys.

that a small number of COSEBIs modes are enough to essentially capture the full cosmological information using numerical analysis and mock data, respectively. Asgari, Schneider & Simon (2012) extended the method to tomographic bins and showed that although a small number of COSEBIs modes is enough for each redshift bin pair, in the presence of many redshift bins, the total number of COSEBIs needed is relatively high. This is also true for all the other conventionally used cosmic shear observables such as the two-point correlation functions or the convergence power spectrum.

The most common approach to estimate covariance matrices is to use mock data from numerical simulations, but the precision with which this can be measured decreases with the number of observables (Hartlap, Simon & Schneider 2007; Taylor & Joachimi 2014; Sellentin & Heavens 2016). The requirement to minimize the number of observables prompted Asgari & Schneider (2015) to develop a compression method that reduces this number substantially, without significant loss of information. In this paper, we show the first measurement of these compressed COSEBIs, which are called CCOSEBIs. We also present the first measurement of tomographic COSEBIs.

CFHTLenS is a 3D weak lensing survey, analysing u^*, g', r', i', z' multiband data spanning 154 deg^2 from the CFHT Legacy Survey Wide Programme. Observed in sub-arcsecond seeing conditions, this survey was optimized for weak lensing science. Pixel-level data processing used the lensing-quality THELI data reduction package (Erben et al. 2013). PSF Gaussianized photometry provided precise photometric redshift distributions (Hildebrandt et al. 2012) with a reasonable level of accuracy as scrutinized in Choi et al. (2016) using a spectroscopic galaxy cross-correlation clustering analysis. Weak lensing shear measurements were derived and calibrated using the *lens*fit Bayesian model-fitting method (Miller et al. 2013). A series of detailed systematics analyses were applied to the full data set, resulting in the rejection of a quarter of the survey area in order to satisfy strict systematic criteria (Heymans et al. 2012).

A number of different cosmological analyses have been carried out using CFHTLenS. Kilbinger et al. (2013) performed a 2D analysis of the data using several cosmic shear estimators, including COSEBIs, the statistic that forms the focus of this work. This 2D analysis was extended by Fu et al. (2014) who used COSEBIs in conjunction with the third-order aperture mass statistic to constrain cosmological parameters. Aside from the analysis of CFHTLenS, Huff et al. (2014) applied COSEBIs on Sloan Digital Sky Survey (SDSS) data to constrain σ_8 and $\Omega_{\rm m}h^2$.

Analyses of CFHTLenS that incorporated the redshift dependence of the weak lensing signal started with a two-bin tomographic analysis in Benjamin et al. (2013) and Simpson et al. (2013). This was followed by a finer six-bin tomographic analysis in Heymans et al. (2013), where the data were modelled as a combination of a cosmological signal and a contaminating signal from the presence of intrinsic galaxy alignments (see also MacCrann et al. 2015; The Dark Energy Survey Collaboration et al. 2015, Joudaki et al. 2016, for re-analyses of this data set). These statistical analyses were based on measurements of the two-point shear correlation functions (2PCFs). Using only blue galaxies, for which the intrinsic alignment contamination is expected to be negligible, Kitching et al. (2014) carried out a full 3D power spectrum analysis of the survey. This power spectrum analysis was restricted to relatively large physical scales to minimize the effects of baryon feedback on the non-linear matter power spectrum (see Semboloni, Hoekstra & Schaye 2013; Harnois-Déraps et al. 2015; Mead et al. 2015, for example). As shown in Kilbinger (2015), there is excellent consistency between the different cosmological constraints derived by these varied statistical analyses of the CFHTLenS survey. The most stringent one, and also the most in tension with the CMB results is the six-bin tomographic analysis of Heymans et al. (2013). We therefore focus our systematics analysis on this tomographic data set.

This paper is structured as follows. Section 2 outlines the statistical methods, COSEBIs and CCOSEBIs that are used in this analysis. Section 3 contains the main results, where we show the measured COSEBIs and CCOSEBIs. We quantify the measured B-modes using a χ^2 analysis and finally conclude in Section 4. We verify our pipeline tests on mock data in the Appendix A.

2 METHODS: COSEBIs AND CCOSEBIs

Converting a measured gravitational lensing shear field to a convergence field does not necessarily result in the real projected mass field expected from gravitational lensing theory (see Bartelmann & Schneider 2001, for a review of weak gravitational lensing). The reason is that aside from first-order lensing effects there are other influential factors. These other factors fall into two categories according to whether their origin is physical or non-physical. The former may arise from higher order lensing effects (contributions beyond the Born approximation, see Schneider et al. 1998) and source redshift clustering (Schneider et al. 2002) or intrinsic galaxy alignments (see Blazek, McQuinn & Seljak 2011, and references therein); The latter case involves noise contributions and remaining systematic effects, for example, in galaxy shape measurements. First-order weak gravitational lensing can only produce modes that are commonly referred to as E-modes, whereas, the modes that arise from the imaginary part of the estimated convergence field, κ, are called B-modes. These modes are so named because of the similar mathematical properties of the shear field and the polarization of an electromagnetic radiation field (both of them are polars). B-mode contributions from physical effects are expected to be negligible for a survey such as CFHTLenS. Hence any detection of a B-mode will arise from either inaccuracies in the shape measurements and/or selection biases. Since the physical contributions to the B-modes are very small, measuring a statistically zero B-mode, suggests (but does not guarantee) a satisfactory PSF correction. Separating these modes is essential to test for systematic errors.

Any observable (statistic) that separates E-modes from B-modes at the two-point statistics level, can be written in the following form,

$$E = \frac{1}{2}\int_0^\infty {\rm d}\vartheta\ \vartheta\ [T_+(\vartheta)\xi_+(\vartheta) + T_-(\vartheta)\xi_-(\vartheta)],$$

$$B = \frac{1}{2}\int_0^\infty {\rm d}\vartheta\ \vartheta\ [T_+(\vartheta)\xi_+(\vartheta) - T_-(\vartheta)\xi_-(\vartheta)], \quad (1)$$

where $\xi_\pm(\vartheta)$ are the two-point correlation functions (2PCFs) of the shear field, ϑ is the angular distance between pairs of galaxies on the sky and $T_\pm(\vartheta)$ are filter functions that are chosen to produce pure E/B-modes, corresponding to E/B, respectively. In Schneider & Kilbinger (2007), conditions for such filters were obtained,

$$\int_{\vartheta_{\rm min}}^{\vartheta_{\rm max}} \frac{{\rm d}\vartheta}{\vartheta}\ T_-(\vartheta) = 0 = \int_{\vartheta_{\rm min}}^{\vartheta_{\rm max}} \frac{{\rm d}\vartheta}{\vartheta^3}\ T_-(\vartheta), \quad (2)$$

$$\int_{\vartheta_{\rm min}}^{\vartheta_{\rm max}} {\rm d}\vartheta\ \vartheta\ T_+(\vartheta) = 0 = \int_{\vartheta_{\rm min}}^{\vartheta_{\rm max}} {\rm d}\vartheta\ \vartheta^3\ T_+(\vartheta), \quad (3)$$

where $\vartheta_{\rm min} > 0$ and $\vartheta_{\rm max}$ is finite. Using these conditions Schneider et al. (2010) constructed two complete orthogonal sets of filter functions, $T_\pm$ that form the basis of the COSEBIs.

2.1 COSEBIs

The two sets of COSEBIs basis functions are the Lin- and Log-COSEBIs, which are written in terms of polynomials in ϑ and $\ln(\vartheta)$ in real space, respectively. In addition to Schneider et al. (2010), Fu & Kilbinger (2010) constructed filters that maximized the signal-to-noise ratio for a specific angular range or maximized the information content of E statistics via Fisher analysis. In this analysis we use the Log-COSEBIs, as they require fewer modes compared to the Lin-COSEBIs to essentially capture all the information (see Schneider et al. 2010 for a single redshift bin and Asgari et al. 2012 for the tomographic case).

The COSEBIs can be written in terms of the 2PCFs in real space,

$$E_n^{(ij)} = \frac{1}{2}\int_{\theta_{\rm min}}^{\theta_{\rm max}} {\rm d}\vartheta\ \vartheta\ \left[T_{+n}(\vartheta)\,\xi_+^{(ij)}(\vartheta) + T_{-n}(\vartheta)\,\xi_-^{(ij)}(\vartheta)\right], \quad (4)$$

$$B_n^{(ij)} = \frac{1}{2}\int_{\theta_{\rm min}}^{\theta_{\rm max}} {\rm d}\vartheta\ \vartheta\ \left[T_{+n}(\vartheta)\,\xi_+^{(ij)}(\vartheta) - T_{-n}(\vartheta)\,\xi_-^{(ij)}(\vartheta)\right], \quad (5)$$

where $E_n^{(ij)}$ and $B_n^{(ij)}$ are the E- and B-mode COSEBIs for redshift bins i and j, $T_{\pm n}(\vartheta)$ are the COSEBIs filter functions and n, a natural number, is the order of the COSEBIs modes. The modes with larger n values are typically more sensitive to small-scale variations in the shear 2PCFs, while the modes with small n are sensitive to large-scale variations. This is because $T_{\pm n}$ are oscillatory functions with $n + 1$ roots in their range of support. Alternatively, the E/B-COSEBIs can be expressed as a function of the convergence power spectra:

$$E_n^{(ij)} = \int_0^\infty \frac{{\rm d}\ell\,\ell}{2\pi} P_{\rm E}^{(ij)}(\ell) W_n(\ell), \quad (6)$$

$$B_n^{(ij)} = \int_0^\infty \frac{{\rm d}\ell\,\ell}{2\pi} P_{\rm B}^{(ij)}(\ell) W_n(\ell), \quad (7)$$

where $P_{\rm E(B)}^{(ij)}$ are the E(B)-mode convergence power spectra and the $W_n(\ell)$ are the Hankel transform of $T_{\pm n}(\vartheta)$

$$\begin{aligned} W_n(\ell) &= \int_{\vartheta_{\rm min}}^{\vartheta_{\rm max}} {\rm d}\vartheta\ \vartheta\ T_{+n}(\vartheta){\rm J}_0(\ell\vartheta) \\ &= \int_{\vartheta_{\rm min}}^{\vartheta_{\rm max}} {\rm d}\vartheta\ \vartheta\ T_{-n}(\vartheta){\rm J}_4(\ell\vartheta), \end{aligned} \quad (8)$$

with $\rm J_0$ and $\rm J_4$ as the ordinary Bessel functions of zeroth and fourth order.

We use equation (6) to find the theory value of the E-mode COSEBIs as most theories provide us with an input power spectrum. However, in practice, the shear 2PCFs are more straightforward to measure from data, hence, equations (4) and (5) are used to calculate the E/B-mode COSEBIs from data and simulations.

2.2 Compressed COSEBIs: CCOSEBIs

Data compression is a challenge that will become increasingly more important for future large-scale surveys such as Euclid[2] and LSST.[3] The main reason data compression is essential is that the number of simulations needed to estimate the data covariance matrix accurately depends on the number of observables. Therefore, having a smaller set of observables reduces the number of cosmological simulations needed.

[2] http://sci.esa.int/euclid/, Laureijs et al. (2011)
[3] http://www.lsst.org/lsst/

Asgari & Schneider (2015) developed a compression method that is based on the sensitivity of observables (statistics) to the parameters to be measured. This method relies on our understanding of these parameters, since the compressed observables depend on the covariance and derivatives of the parent observable to the parameters at their fiducial value. The assumption behind this compression method is that we have a relatively good idea of the value of the parameters that we want to measure (for example from previous observations), which is correct for most of the cosmological parameters. One might expect to lose a significant portion of the information about the parameters if the fiducial covariance matrix used for constructing the parameters is not close to the truth. However, Asgari & Schneider (2015) applied this compression method to tomographic COSEBIs and showed that the weak lensing information lost due to this compression is small even for very inaccurate COSEBIs covariance matrices. This implies that this compression is insensitive to the inaccuracies in the estimated covariance matrix of the parent observables, which means that using this compression allows for the same accuracy in estimations with fewer cosmological simulations.

Here, we will also use compressed COSEBIs (CCOSEBIs) for the analysis of the CFHTLenS data. The CCOSEBIs are linear combinations of the COSEBIs. The coefficients of these linear combinations are written in terms of the covariance and the derivatives of the COSEBIs with respect to cosmological parameters,

$$\boldsymbol{E}^{\rm c} = \boldsymbol{\Gamma}\,\boldsymbol{E}, \quad (9)$$

where $\boldsymbol{E}^{\rm c}$ is the E-mode CCOSEBIs vector, $\boldsymbol{E}$ is the E_n^{ij} vector and $\boldsymbol{\Gamma}$ is the compression matrix defined as,

$$\boldsymbol{\Gamma} \equiv \mathbf{H}\mathbf{C}^{-1}, \quad (10)$$

where $\mathbf{H}$ is a matrix formed of both first and second derivatives of the COSEBIs with respect to the cosmological parameters and $\mathbf{C}$ is the covariance matrix of COSEBIs (see section 2 of Asgari & Schneider 2015, for the details of the formalism). The number of CCOSEBIs modes for constraining P cosmological parameters is $P(P + 3)/2$, regardless of the number of COSEBIs used. For a total of $\mathcal{N}_{\rm max}$ COSEBIs modes and P parameters, $\boldsymbol{\Gamma}$ is a matrix with $P(P + 3)/2$ rows and $\mathcal{N}_{\rm max}$ columns, where the first P rows are the COSEBIs first-order derivatives while the last $P(P + 1)/2$ rows are the second-order derivative of COSEBIs with respect to the parameters.

3 RESULTS

In this section, we apply two analysis methods, based on COSEBIs and CCOSEBIs, respectively, to measure the cosmic shear signal from CFHTLenS data. Before applying our methods on the data, we performed a number of tests including blind tests on mock data, as explained in Appendix. Appendix also details the technical aspects of calculating the COSEBIs from shear two-point correlation functions.

3.1 Analysis

In order to compare our results with the previous CFHTLenS analysis as well as to test the data for systematic errors in a comprehensive manner, we analyse the data in several different ways. We choose the three angular ranges, [1 arcmin, 40 arcmin], [40 arcmin, 100 arcmin] and [1 arcmin, 100 arcmin] corresponding to small, large and the combination of both angular scales. We also consider two sets of galaxy populations, all and blue galaxies only. The blue galaxies are late-type galaxies and are expected to have a negligible intrinsic

Table 1. Effective number density of galaxies, $n_{\rm eff}$ (arcmin^{-2}), in each redshift bin for late-type (Blue) and all (All) Galaxies.

z-bin	Blue: $n_{\rm eff}$	All: $n_{\rm eff}$
[0.2, 0.39]	1.507	1.811
[0.39, 0.58]	1.265	1.646
[0.58, 0.72]	1.560	1.907
[0.72, 0.86]	1.366	1.788
[0.86, 1.02]	1.440	1.729
[1.02, 1.3]	1.395	1.708
[0.2, 1.3]	8.533	10.589

galaxy alignment signal (see Heymans et al. 2013). This population is selected using their Bayesian photometric redshift spectral type, $T_B > 2$ (see Velander et al. 2014, for the definition). In addition, we compare a 2D, non-tomographic, analysis with a six redshift bins tomographic analysis. Table 1 shows the redshift bins and their corresponding effective number density of galaxies for the blue and all galaxies. The redshift distribution of the CFHTLenS data is measured using photometric redshift estimates as explained in Hildebrandt et al. (2012).

Listed below are the configurations we used in this paper that best resemble the previous two-point statistics cosmic shear analysis of CFHTLenS.

(i) Heymans et al. (2013) performed an analysis with a setup, which corresponds to the tomographic [1 arcmin, 40 arcmin] angular range with all galaxies. They modelled galaxy intrinsic alignments with a single parameter, as the intrinsic-shear signal is non-negligible when all galaxies are considered in tomographic bins.

(ii) Kitching et al. (2014) used large scales (roughly the [40 arcmin, 100 arcmin] range) with blue galaxies. They used 3D cosmic shear analysis in the Fourier space that is approximately equivalent to our tomographic analysis.

(iii) Kilbinger et al. (2013) used a large range of scales for their analysis that is close to the [1 arcmin, 100 arcmin] range we consider. Their analysis considered all galaxies without any redshift binning.

In this analysis, we choose to ignore the CFHTLenS photometric redshift biases and uncertainties presented in Choi et al. (2016) in order to be able to directly compare our results to the CFHTLenS analyses listed above. Joudaki et al. (2016) investigated the effect of the redshift biases and showed that the effect is small on the cosmological information. The B-mode analysis, which is the main subject of this work, is essentially unaffected by the redshift measurement biases.

3.2 Cosmological models

The cosmological models we compare our results to are two flat ΛCDM models, with parameters corresponding to the best-fitting values of CFHTLenS+*WMAP*7 (Heymans et al. 2013) and *Planck* TT+ lowP (Planck Collaboration et al. 2016a). We assume a primordial power-law power spectrum and use the Bond & Efstathiou (1984) transfer function to calculate the linear matter power spectrum. The non-linear power spectrum is estimated using the halo fit formula of Smith et al. (2003). MacCrann et al. (2015) show that this choice of non-linear fitting function does not significantly change cosmological parameter constraints with CFHTLenS, in comparison to analyses that use improved non-linear correction schemes (Takahashi et al. 2012; Mead et al. 2015).

Table 2. Cosmological parameters for a flat ΛCDM cosmology. The first row corresponds to CFHTLenS+*WMAP*7 best-fitting values, the second row belongs to *Planck* best-fitting values for TT+lowP and the final row shows the values for the SLICS simulations.

	σ_8	$\Omega_{\rm m}$	$n_{\rm s}$	h	$\Omega_{\rm b}$
CF+WM	0.794	0.255	0.967	0.717	0.0437
Planck	0.829	0.315	0.9655	0.6731	0.0490
SLICS	0.826	0.2905	0.969	0.6898	0.0473

The cosmological parameters are given in Table 2, where we also show the parameters for the simulation products that are used for pipeline verifications as well as estimating the covariances. The cosmological parameters that are presented in Table 2 are, σ_8, the normalization of the matter power spectrum, $\Omega_{\rm m}$, the mean matter density parameter, $n_{\rm s}$, the spectral index, h, the dimensionless Hubble parameter and $\Omega_{\rm b}$, the baryonic matter density parameter. Spatial flatness is assumed throughout out this work, which means that $\Omega_\Lambda = 1 - \Omega_{\rm m}$, where Ω_Λ is the dark energy density parameter.

3.3 Covariance

The covariance matrix of the COSEBIs is measured from mock galaxy catalogues constructed from the SLICS, a suite of N-body simulations described in Harnois-Déraps & van Waerbeke (2015). The mock galaxy population algorithm, detailed in Joudaki et al. (2016), is designed to reproduce the properties of the CFHTLenS catalogues. These new mock catalogues are updated versions of those used in the previous analysis of the CFHTLenS, which offer better precision especially at large angular scales, since the box size of the simulations is $L = 505$ Mpc h^{-1}; which is significantly larger than the simulation set used for modelling the earlier CFHTLenS measurements ($L = (147,231)$ Mpc h^{-1}), hence, the new simulation set is less affected by suppression of the large-scale variance by finite box size effects. Furthermore, we use 497 in comparison to the 184 independent simulations used in the earlier work.

Estimating covariances from a finite number of simulations is noisy that causes biases in the inverse covariance (see Hartlap et al. 2007). Assuming Gaussian errors on the estimated covariance matrix, $\hat{\mathbf{C}}$, the inverse covariance matrix is given by

$$\mathbf{C}^{-1} = \frac{n_{\rm sim} - n_{\rm obs} - 2}{n_{\rm sim} - 1}\hat{\mathbf{C}}^{-1}, \tag{11}$$

where $n_{\rm sim}$ and $n_{\rm obs}$ are the number of simulations and observables, respectively. For $n_{\rm obs}/n_{\rm sim} < 0.8$, the above formula produces an unbiased inverse covariance according to Hartlap et al. (2007). It will however still have noise associated with it, which depends on the ratio of the number of observables to the number of simulations. Taylor & Joachimi (2014) extended this analysis by providing a more accurate correction for the parameter covariance matrix as

$$\mathbf{C}_{\rm par} = \frac{n_{\rm sim} - n_{\rm obs} - 2}{n_{\rm sim} - n_{\rm obs} + n_{\rm par} - 1}\hat{\mathbf{C}}_{\rm par}, \tag{12}$$

where $\mathbf{C}_{\rm par}$ is the parameter covariance matrix and $n_{\rm par}$ is the number of parameters to be estimated. Applying this correction to $\mathbf{C}_{\rm par}$ results in a slightly smaller covariance matrix in comparison to the Hartlap et al. (2007) method, for $n_{\rm par} \ll (n_{\rm sim} - n_{\rm obs})$, but there is still noise associated with it. Sellentin & Heavens (2016) extended this analysis further to mitigate covariance matrix estimation uncertainties by marginalizing over the true covariance matrix given its estimated value. They show improvements over the Hartlap et al.

(2007) and Taylor & Joachimi (2014) estimate, by noting that their corrected covariance matrix distribution is no longer Gaussian.

In our analysis, the maximum number of observables that we use is $7 \times 21 = 147$ COSEBIs modes, where 7 is the number of COSEBIs modes in each redshift pair and 21 is the number of redshift pairs for the tomographic case. As a result the ratio $n_{\rm obs}/n_{\rm sim} \approx 0.3$, which can cause about 7 per cent errors in the estimated inverse covariance using the Hartlap et al. (2007) correction. This value for the error on the covariance matrix is acceptable for analysing CFHTLenS data around the maximum likelihood point. However, around the tails of the likelihood distribution the Sellentin & Heavens (2016) correction becomes significant. Therefore, we apply this correction in Section 3.5, where we calculate the p-values, primarily to assess the significance of the detected B-modes.

3.4 Measurements

Following Heymans et al. (2012), we analyse the 129 CFHTLenS fields that passed the systematic tests, representing 75 per cent of the total observed area.

We calibrate the data correcting for additive and multiplicative biases between the observed, $\epsilon_{\rm obs}$, and the true ellipticities, $\epsilon_{\rm true}$, modelled as

$$\epsilon_{\rm obs} = (1+m)\,\epsilon_{\rm true} + c, \tag{13}$$

where ϵ is a complex quantity defined as $\epsilon = \epsilon_1 + i\epsilon_2$, where ϵ_1 and ϵ_2 are real quantities.

In CFHTLenS analyses, c was measured to be zero and 2×10^{-3} on average for ϵ_1 and ϵ_2, respectively. The origin of the additive bias is unknown and its value is calibrated from the data empirically. It is likely that the multiplicative bias, m, originates from the effect of noise in shape measurements (see for example Melchior & Viola 2012). It is estimated from galaxy image simulations. While the additive bias is subtracted from the observed ϵ_2 directly, the effect of the multiplicative bias is applied globally as explained in Miller et al. (2013). The measured 2PCFs are divided by the calibration function

$$1 + K(\vartheta) = \frac{\sum_{ab} w_a w_b (1+m_a)(1+m_b)}{\sum_{ab} w_a w_b}, \tag{14}$$

where w_a and m_a are the weight and the multiplicative bias associated with a galaxy at position a. The sum is carried out over all pairs of galaxies with a separation falling within the ϑ bin. Each galaxy has an inverse variance weight associated with it. Less-noisy galaxy shapes have a larger weight value, ergo they are more important in the analysis. The definition of w can be found in Miller et al. (2013).

The estimated 2PCFs, from the input ellipticities and their associated weights, w, for redshift bins i and j, are given by

$$\hat{\xi}_{\pm}^{ij}(\vartheta) = \frac{\sum w_a w_b \left[\epsilon_{\rm t}^i(\boldsymbol{x}_a)\epsilon_{\rm t}^i(\boldsymbol{x}_b) \pm \epsilon_{\rm x}^i(\boldsymbol{x}_a)\epsilon_{\rm x}^i(\boldsymbol{x}_b)\right]}{\sum w_a w_b}, \tag{15}$$

where $\epsilon_{\rm t/x}(\boldsymbol{x}_a)$ are the tangential/cross ellipticities at position $\boldsymbol{x}_a$, with respect to the reference frame connecting the pairs of galaxies involved. $\hat{\xi}_{\pm}^{ij}(\vartheta)$ is then divided by $1 + K(\vartheta)$ to find an unbiased estimate.

To estimate the 2PCFs, we use ATHENA[4] (see Kilbinger, Bonnett & Coupon 2014), a tree code that calculates second-order correlation functions from input galaxy catalogues. The opening angle that we use is 0.02 rad, which shows no significant differences with a brute force (opening angle = 0) estimation.

The estimated 2PCFs are then inserted into equations (4) and (5) to determine the COSEBIs E- and B-modes, respectively (the details of which are explained in the Appendix). The theory values of COSEBIs are estimated using equations (6) and (7) that relate the COSEBIs to the convergence power spectrum directly. In this analysis, we use the first seven COSEBIs modes, since Asgari et al. (2012) have shown that these are enough to essentially capture the full information for up to seven cosmological parameters.[5] Assuming tomographic bins each redshift bin pair will have 7 COSEBIs modes that adds up to 147 modes in total. Using the compression method in Asgari & Schneider (2015) we decrease this number to 20.

Fig. 1 shows the measured COSEBIs for a single redshift bin using all galaxies. The panels show the results for the three angular ranges, [1 arcmin, 100 arcmin], [1 arcmin, 40 arcmin] and [40 arcmin, 100 arcmin]. The symbols show the COSEBIs modes estimated from the data, while the theory values are shown as curves. The COSEBIs modes are discrete and the curves are drawn to aid the viewer. The E-mode COSEBIs are shown by black squares while the red circles are the B-modes. The B-modes are shifted to the right to aid the viewer. The errors on the data are estimated from the simulations and are correlated (see the covariance in Fig. A3). As we will see in Section 3.5, the B-modes in this plot are only significant for the angular scale [40 arcmin, 100 arcmin]. The theory E-mode curves belong to CFHTLenS+*WMAP*7 and *Planck* best-fitting values listed in Table 2. We also see that the highest signal-to-noise ratio comes from small scales as expected (see Asgari et al. 2012, for example).

Fig. 2 shows the estimated COSEBIs for the tomographic case with blue galaxies. The E/B-modes are separated into the upper and lower triangle of the plot. Each panel belongs to a redshift bin pair indicated at its corner. Similar to Fig. 1, the measured E- and B-modes are shown as black squares and red circles, respectively. The curves show the theory values of the E-modes for the CFHTLenS+*WMAP*7 and *Planck* cosmologies in Table 2. The angular range considered is [1 arcmin, 100 arcmin]. Unlike the single redshift bin case, we see statistically non-zero B-modes in this figure.

Fig. 3 shows the first measurement of CCOSEBIs from data. We use blue galaxies with six tomographic bins and the three angular ranges to estimate the CCOSEBIs. Here, we choose the five cosmological parameters in Table 2 to compress COSEBIs into 5 first-order and 15 second-order CCOSEBIs, using the *Planck* values as our fiducial cosmology to calculate the compression matrix (see equation 10). The CCOSEBIs modes are named after the parameters that are used to define them, shown on the x-axis. The first-order modes only depend on one cosmological parameter, whereas the second-order CCOSEBIs depend on two parameters that could be the same. For example, the points related to $\Omega_{\rm m}h$ show the value of the second-order CCOSEBIs mode that is based on the derivatives of COSEBIs to $\Omega_{\rm m}$ and h. The ordering of the modes is arbitrary and the apparent oscillations in the figure can be rearranged. The theory values of the CCOSEBIs for CFHTLenS+*WMAP*7 and *Planck*

[4] http://www.cosmostat.org/software/athena/

[5] Depending on the origin of the B-mode systematic, seven COSEBIs modes may not be enough to capture all of the information in the B-mode signal. Further work is required to test different systematic scenarios and how they impact the different COSEBIs. For the purpose of this paper, however, we match our B-mode analysis to the seven modes that are optimal for E-mode measurements.

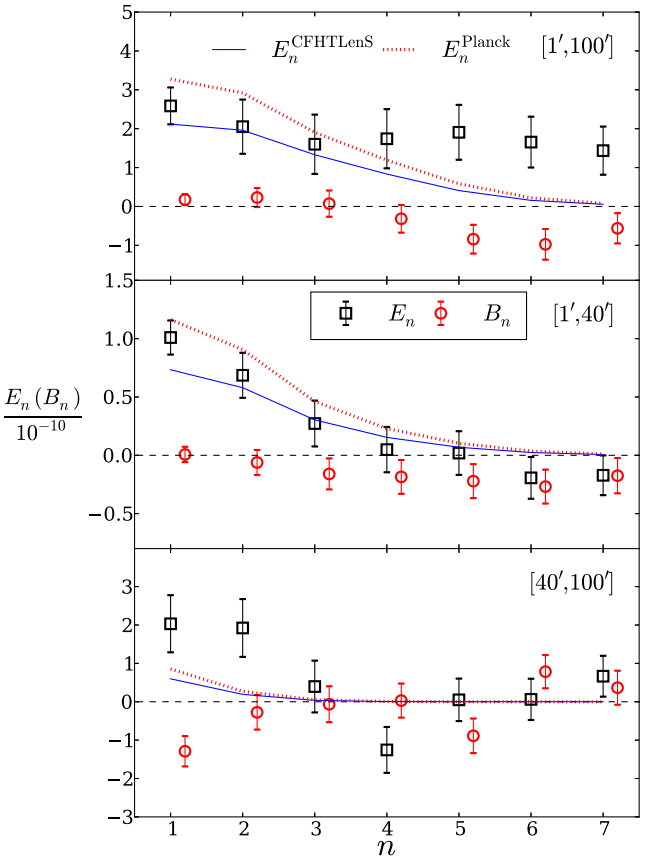

Figure 1. Measured COSEBIs from the CFHTLenS data for a single redshift bin using all galaxies. Three angular ranges are considered here. The dashed line shows the zero B-mode value. The B_n modes (red circles) are shifted to the right for visual assistance. The E_n (black squares) are compared with their theoretical values given the *Planck* (red dotted curve) and CFHTLenS+*WMAP*7 (blue solid curve) cosmologies. The CFHTLenS+*WMAP*7 theoretical values are best-fitting values for the [1 arcmin, 40 arcmin] angular range with tomography (see Heymans et al. 2013). The values of the cosmological parameters for the theoretical curves are given in Table 2. Note that the COSEBIs modes are discrete and the theory values are connected to each other for visual inspection. The errors are estimated from simulated data explained in Appendix A3. Note that the different modes are correlated (see the covariance in Fig. A3).

cosmologies are shown as the blue solid curve and the red dashed curve. Note that the CCOSEBIs modes are discrete and the theoretical values are connected for an easier comparison. The B-modes are shown on the same scale as the E-modes. The CCOSEBIs are designed to be sensitive to cosmological information about these parameters. Therefore, they may not be as sensitive to the B-modes in the data. As we will see for most cases that we have studied, even if there are significant B-modes picked up by COSEBIs, the B-modes are not always significant with the CCOSEBIs. The exception is the [40 arcmin, 100 arcmin] angular range that shows significant B-modes either way.

3.5 Figure of merit and fitting

To quantify the significance of the measured B-modes we estimate their χ^2 value with zero,

$$\chi^2_B = \sum \boldsymbol{B}^{\rm t}\mathbf{C}^{-1}\boldsymbol{B}, \tag{16}$$

where $\boldsymbol{B}$ is a vector composed of B_n, $\boldsymbol{B}^{\rm t}$ is its transpose and $\mathbf{C}^{-1}$ is the inverse of the B-mode covariance matrix, estimated from the SLICS simulations. We also estimate the χ^2 values for the E-modes compared to the best-fitting values of CFHTLenS+*WMAP*7 and *Planck* (see Table 2). The raw value of the χ^2 is not particularly informative, even when the degrees of freedom is known (see Andrae, Schulze-Hartung & Melchior 2010, for example). Hence instead we show the p-values for the estimated χ^2 values. The p-value shows the probability of finding a χ^2 value larger than the one estimated. We choose a significance level of 99 per cent, p-value = 0.01, which corresponds to a deviation of about 2.6σ for a normal distribution. Recall that a χ^2 distribution is skewed towards smaller values and asymptotically reaches a normal distribution for large numbers of degrees of freedom as illustrated in Fig. A6. Additionally, using an inverted noisy covariance changes a χ^2 distribution and hence the derived p-values, which we account for using the method proposed by Sellentin & Heavens (2016).

Fig. 4 shows the p-values for the COSEBIs B_n versus $n_{\rm max}$, the maximum number of COSEBIs used starting from the first mode. The p-values are shown for the three configurations that are closest to the previous CFHTLenS analysis described in Section 3.1. The grey circles correspond to [1 arcmin, 100 arcmin] range without tomography and with all galaxies, which resembles Kilbinger et al. (2013). The blue squares belong to [40 arcmin, 100 arcmin] angular range with tomography and blue galaxies similar to Kitching et al. (2014). The diamonds configuration is the same as Heymans et al. (2013), where all galaxies in the angular range [1 arcmin, 40 arcmin] are considered and binned in redshift. In this plot, we see that the p-values for the single redshift bin case are always above 0.01, which means that they are insignificant. In contrast, on large scales, the B-modes are always below 0.01 and are significant. In addition, the tomographic analysis using the lower angular range, [1 arcmin, 40 arcmin] also shows insignificant B-modes with a p-value above 0.01. When we use CCOSEBIs, the B-modes significance decreases, as we will see in Table 3.

Table 3 shows the p-values for all the cases that we have considered. The first four columns indicate the setup, while the last six show the p-values for that setup for, $B_n = 0$, $E_n = E_n^{\rm CFHTLenS}$, $E_n = E_n^{\rm Planck}$, $B^c = 0$, $E^c = E^{\rm c,\,CFHTLenS}$ and $E^c = E^{\rm c,\,Planck}$, respectively. The p-values for CCOSEBIs are only shown for the tomographic cases where CCOSEBIs offers a compression. The $n_{\rm max}$ column shows the number of COSEBIs modes in each redshift bin that are used in the analysis. We show the results for both the first two and seven COSEBIs. The p-values are written in boldface where they are larger than 0.01 that corresponds to the significance level within 99 per cent. Looking at the B_n column and the single redshift bin cases, we see that the B-modes are only significant at large scales ([40 arcmin, 100 arcmin]). When redshift binning is considered, with the exception of the [1 arcmin, 40 arcmin] case there are significant B-modes in the data. The B-modes are not always consistent between the two galaxy populations, which hints at a correlation between galaxy colour and residual systematics. Also notice that the largest scales show significant B-modes for all the different sets of data analysed.

The B^c column shows the CCOSEBIs B-modes that are typically less significant than that of COSEBIs. As discussed before, this is due to the fact that the CCOSEBIs are based on linear combinations of COSEBIs that are most sensitive to cosmological parameters. They are therefore not necessarily sensitive to the B-modes which, for CFHTLenS, appear to cancel to some degree with the compressed form of the statistic. Consequently, to measure B-modes

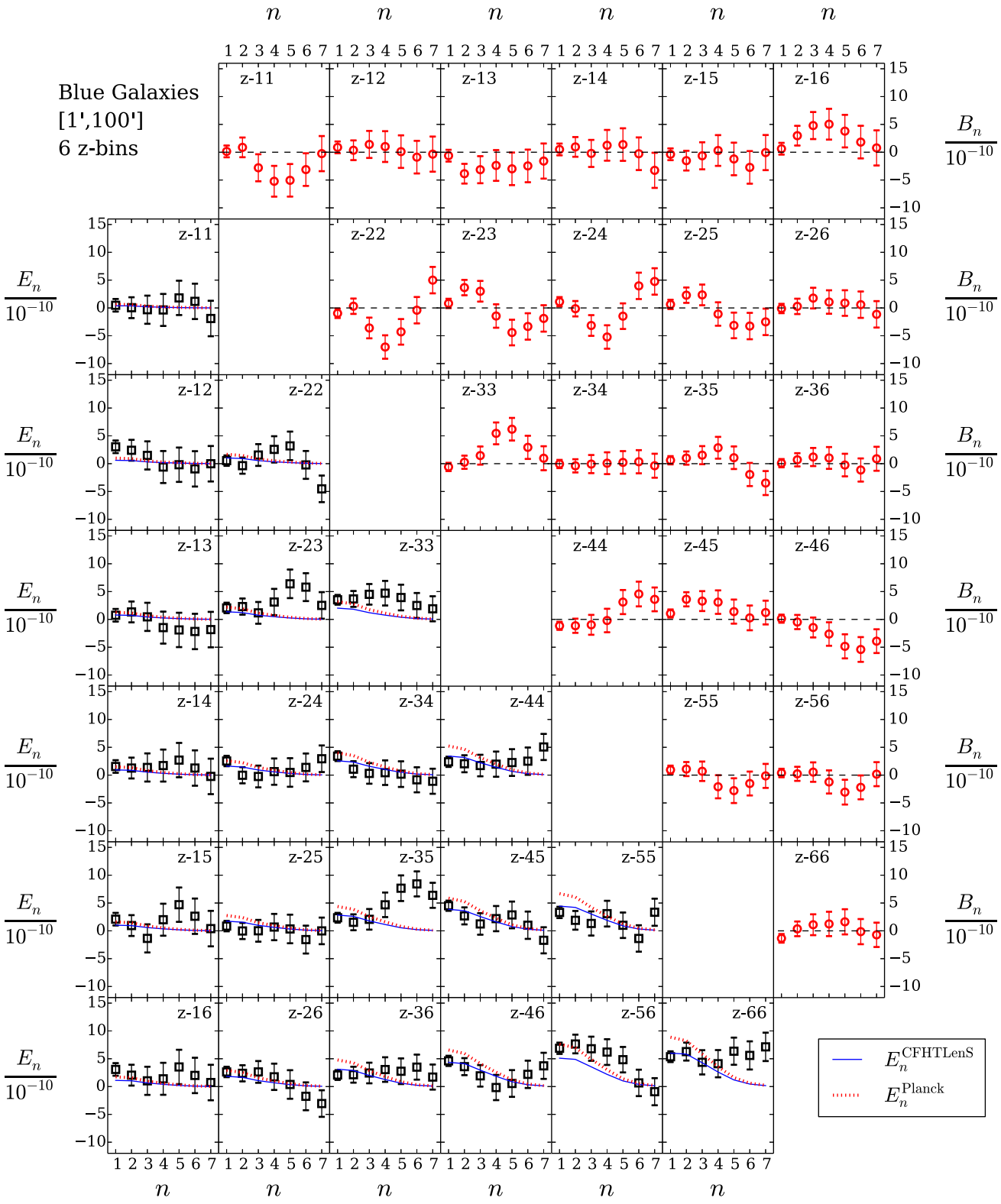

Figure 2. Measured COSEBIs from the CFHTLenS data for six redshift bins using blue galaxies. The angular range [1 arcmin, 100 arcmin] is used here. The B-modes (red circles) are shown in the upper right triangle, while the E-modes (black squares) are shown in the lower left triangle for the redshift bin pairs indicated for each panel. The theoretical values of E_n are shown for the *Planck* (red dotted curve) and CFHTLenS+*WMAP*7 (blue solid curve) cosmologies (see Table 2). Note that the COSEBIs modes are discrete and the theoretical values are connected to each other for visual inspection. The errors are estimated from the mock data explained in Appendix A3. Note that the different modes are correlated as shown in Fig. A4.

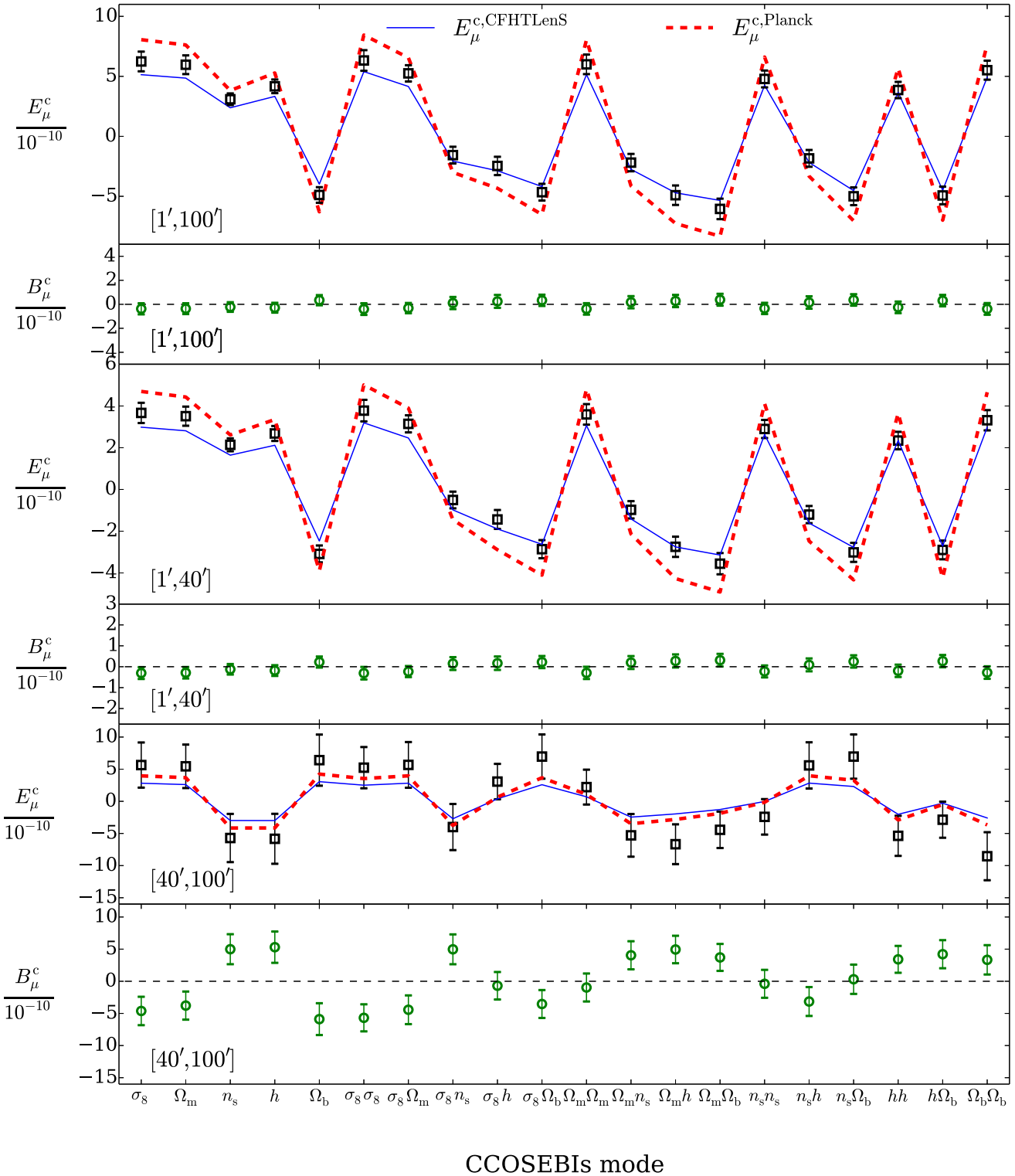

Figure 3. Measured CCOSEBIs from the CFHTLenS data for six redshift bins using blue galaxies. The B-modes are shown as green circles. The black dashed line shows where the zero line for the B-modes lies. The measured E-modes are shown as black squares, while the theory values corresponding to the best-fitting values for CFHTLenS+*WMAP*7 and *Planck* (see Table 2) cosmologies are shown as blue solid curves and red dotted curves, respectively. Note that the CCOSEBIs modes are discrete and the theory values are connected to each other for visual inspection. The errors are estimated from simulated data explained in Appendix A3. Note that the different modes are correlated (see the covariance in Fig. A5).

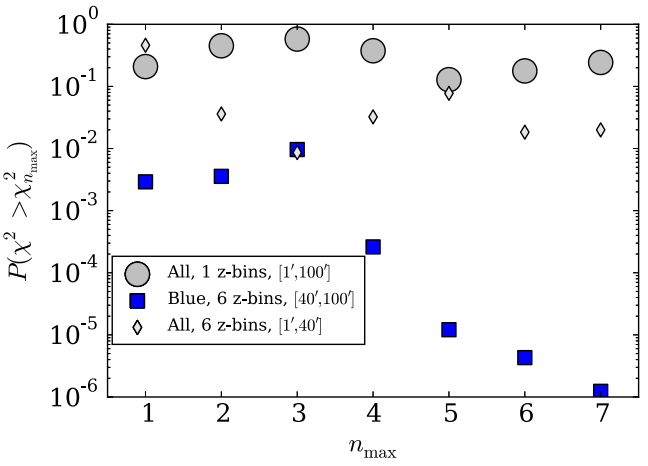

Figure 4. p-values for χ^2 of B-mode compared to zero versus the number of COSEBIs modes. $n_{\rm max}$ denotes the number of COSEBIs modes from $n = 1$ to $n = n_{\rm max}$. The p-value is the probability of the χ^2 value being larger than the value found, assuming $B_n = 0$ is the model. A very small p-value shows a poor agreement between the theory and the estimated values. We reject the null hypothesis (zero B-modes) for p-values smaller than 0.01, which corresponds to a significance larger than 99 per cent. The blue squares show the results for blue galaxies with six redshift bins for the largest angular scales, the light diamond belong to all galaxies with six redshift bins and small angular scales. Finally, the grey circles show the p-values for all galaxies, a single redshift bin and the [1 arcmin, 100 arcmin] range.

we need to use COSEBIs, which provide a complete set of functions for this analysis.

Comparing the $E_n^{\rm CFHTLenS}$ and $E_n^{\rm Planck}$ columns we see that *Planck* provides a better match to the single redshift bin data for all the cases.[6] However, when tomography is considered the CFHTLenS cosmology provides a better match with the exception of the very large scales. For blue galaxies at [40 arcmin, 100 arcmin] the p-values for $E_n^{\rm CFHTLenS}$ and $E_n^{\rm Planck}$ are comparable. We also note that for many tomographic cases, neither provide a good match. When all galaxies are considered, we need to add intrinsic alignment corrections to our model as was done in Heymans et al. (2013). However, for blue galaxies, the contribution from intrinsic alignment is expected to be small; hence, we expect and find a good fit to the CFHTLenS values.

3.6 Single parameter fit

We use a very simple parametrization to fit the theory to data, consisting of one free parameter. We find its best-fitting value by minimizing its χ^2 value and the error to the fit corresponds to the parameter value at $\Delta\chi^2 = 1$ around the minimum χ^2. For the B-modes, the single parameter model we use is a constant:

$$B_n = K_B, \qquad \text{and} \qquad B^{\rm c} = K_{B^{\rm c}}, \tag{17}$$

for COSEBIs and CCOSEBIs, respectively. For the E-modes, the models are a constant, times the theory E-modes, with CFHTLenS+*WMAP*7 and *Planck* cosmologies. For COSEBIs these are

$$E_n = K_{\rm E}^{\rm CFHTLenS} E_n^{\rm CFHTLenS}, \tag{18}$$

and

$$E_n = K_{\rm E}^{\rm Planck} E_n^{\rm Planck}, \tag{19}$$

whereas for CCOSEBIs

$$E^{\rm c} = K_{\rm E^c}^{\rm CFHTLenS} E^{\rm c,CFHTLenS}, \tag{20}$$

and

$$E^{\rm c} = K_{\rm E^c}^{\rm Planck} E^{\rm c,Planck}, \tag{21}$$

are the two models. The best-fitting and error values for $K_{\rm B}$, $K_{\rm E}^{\rm CFHTLenS}$, $K_{\rm E}^{\rm Planck}$, $K_{\rm B^c}$, $K_{\rm E^c}^{\rm CFHTLenS}$, $K_{\rm E^c}^{\rm Planck}$ are listed in Table 4. The format of this table is the same as Table 3. Null B-modes result in a statistically zero $K_{\rm B}$; however, a statistically zero $K_{\rm B}$ is not a sufficient condition for B-modes to be zero. The rows for which the COSEBIs B-modes are consistent with zero from the p-value test are shown in boldface. Some of the $K_{\rm B}$ values that are consistent with zero in this table correspond to significant B-modes from the p-value test. This shows that the B-mode pattern in the data is not always well modelled by a constant value.

3.7 Comparison to previous analyses

Tables 3 and 4 allow us to compare our results with the previous CFHTLenS cosmic shear analysis. We first consider Heymans et al. (2012) who detail a systematics test using an E–B mode decomposition for three different two-point statistics; the top-hat shear variance, the 2PCF and the mass aperture statistics. Analysing angular scales from [1 arcmin, 60 arcmin] applying no redshift binning, they found no significant B-modes, which is consistent with our results.

Kilbinger et al. (2013) performed a 2D analysis of the data using several cosmic shear methods, including the COSEBIs. The aim of their work was to use a large angular range to estimate cosmological parameters; but, they faced difficulties estimating the COSEBIs from their mock data, known as the Clone simulations. The main reason for their difficulties was the fact that the accuracy of the simulations for very large angular scales is limited due to the finite box size. Consequently, they did not use COSEBIs for their final analysis of the data. Here, we used updated simulations (SLICS) with better accuracy for large scales and did not encounter similar problems. We compare their results with our [1 arcmin, 100 arcmin] angular range with all galaxies and a single redshift bin. They reported insignificant B-modes that is consistent with our results.

Kitching et al. (2014) restricted their study to large scales and blue galaxies with redshift information. They reported no significant B-modes. Although the scales they used are defined in the Fourier space where they performed their analysis, they roughly correspond to the large scales that we have considered here. In contrast to their study we find very significant B-modes in the [40 arcmin, 100 arcmin] range. One reason for this inconsistency could be that their mask model lacks the precision to find the B-modes (see Asgari et al., in preparation, for mask modelling). In contrast to power spectrum analysis, mask modelling has little or no effect on the estimation of COSEBIs. Alternatively, this inconsistency could be due to the complexity of translating the angular ranges used in a COSEBIs analysis to the Fourier modes considered in 3D-lensing.

Our best-fitting CFHTLenS+*WMAP*7 fiducial cosmology comes from Heymans et al. (2013), who used the [1 arcmin, 40 arcmin] range with tomography. They did not incorporate any E/B-mode

[6] Here, we use p-values as a proxy for χ^2 values, which would be used in sampling the parameter likelihood in a typical cosmological analysis. We will not attempt to reject either $E_n^{\rm CFHTLenS}$ or $E_n^{\rm Planck}$ using this method or quantify their tension.

Table 3. p-values for χ^2 of $B_n = 0$, $E_n = E_n^{\rm CFHTLenS}$, $E_n = E_n^{\rm Planck}$, $B^c = 0$, $E^c = E^{\rm c,\,CFHTLenS}$ and $E^c = E^{\rm c,\,Planck}$. The p-values denote the probability of the χ^2 values being larger than the values found, assuming the model is correct. Each row corresponds to a different angular range (θ range), group of galaxies (Galaxies), number of redshift bins (z-bins) and number of COSEBIs modes ($n_{\rm max}$) considered in the analysis. The CCOSEBIs p-values are only shown for the tomographic case where the number of CCOSEBIs modes is smaller than that of COSEBIs. The P-values that are larger than 0.01 are shown in boldface and lie within the 99 per cent confidence limit. See Table B1 for the χ^2 values and degrees of freedom for each entry in this table.

				COSEBIs			CCOSEBIs		
θ range	Galaxies	z-bins	$n_{\rm max}$	B_n	$E_n^{\rm CFHTLenS}$	$E_n^{\rm Planck}$	$B^{\rm c}$	$E^{\rm c,\,CFHTLenS}$	$E^{\rm c,\,Planck}$
[1 arcmin − 100 arcmin]	All	1	2	**4.5e − 01**	**1.6e − 01**	**3.4e − 01**	–	–	–
			7	**2.4e − 01**	**4.5e − 02**	**2.1e − 01**	–	–	–
		6	2	2.0e − 03	3.3e − 03	4.6e − 04	**3.5e − 02**	**7.8e − 02**	**1.1e − 02**
			7	6.6e − 03	6.1e − 04	2.0e − 04	**8.0e − 01**	4.8e − 04	2.5e − 04
	Blue	1	2	**2.1e − 01**	**6.8e − 02**	**3.5e − 01**	–	–	–
			7	**2.2e − 01**	2.1e − 03	**1.3e − 02**	–	–	–
		6	2	4.4e − 04	**3.5e − 02**	5.7e − 03	**6.0e − 02**	**2.7e − 01**	**6.7e − 02**
			7	3.9e − 03	9.7e − 03	4.9e − 03	**4.7e − 01**	**1.1e − 01**	**3.5e − 02**
[1 arcmin − 40 arcmin]	All	1	2	**7.4e − 01**	**3.2e − 02**	**5.1e − 01**	–	–	–
			7	**7.4e − 01**	**1.2e − 01**	**5.0e − 01**	–	–	–
		6	2	**3.6e − 02**	3.0e − 03	1.3e − 03	**2.5e − 01**	**3.2e − 02**	**1.1e − 02**
			7	**2.0e − 02**	6.8e − 03	1.9e − 03	**6.2e − 01**	4.2e − 03	1.3e − 03
	Blue	1	2	**6.5e − 01**	**1.8e − 02**	**8.8e − 01**	–	–	–
			7	**2.7e − 01**	3.2e − 03	**2.4e − 02**	–	–	–
		1	2	**3.8e − 02**	**2.4e − 02**	**1.2e − 02**	**7.0e − 01**	**3.2e − 01**	**2.0e − 01**
			7	**2.7e − 01**	8.9e − 03	2.6e − 03	**7.6e − 02**	**1.4e − 01**	**5.7e − 02**
[40 arcmin − 100 arcmin]	All	1	2	4.4e − 03	**4.0e − 02**	**6.9e − 02**	–	–	–
			7	2.4e − 03	**6.2e − 02**	**8.7e − 02**	–	–	–
		6	2	1.1e − 03	**1.2e − 02**	**1.6e − 02**	**4.8e − 02**	4.5e − 03	5.9e − 03
			7	1.8e − 06	4.7e − 06	5.3e − 06	**3.5e − 02**	6.4e − 03	8.9e − 03
	Blue	1	2	5.5e − 03	**1.5e − 01**	**2.1e − 01**	–	–	–
			7	2.9e − 03	**4.4e − 02**	**5.5e − 02**	–	–	–
		6	2	3.6e − 03	**6.7e − 02**	**7.4e − 02**	7.3e − 04	**1.1e − 01**	**1.2e − 01**
			7	1.2e − 06	1.1e − 04	1.1e − 04	9.6e − 04	**1.7e − 01**	**1.8e − 01**

decomposition methods in their analysis since they used 2PCFs to find their best-fitting values. For the angular range they used, we find significant B-modes when all galaxies and seven COSEBIs modes are considered. When only two COSEBIs modes are considered, or only using blue galaxies, the B-modes are consistent with zero. Considering blue galaxies only where intrinsic alignments are not important, we see that our measurements favour their best-fitting values in comparison to *Planck*. In particular, the CCOSEBIs matches to both theoretical values for this case; however, the CFHTLenS+*WMAP*7 is a better match, as expected. Aside from our choice of observables and the modelling of the intrinsic alignments, there are no other differences between our study and Heymans et al. (2013).

Fu et al. (2014) added three-point statistics to the Kilbinger et al. (2013) 2D analysis and found significant B-modes in their third-order statistics. Our findings combined with theirs show that there are still (high-order) residual systematic errors left in the CFHTLenS data.

4 CONCLUSIONS

In this paper, we revisited the CFHTLenS data and found evidence for systematic errors on large scales, and when the data are analysed in tomographic bins. We used COSEBIs, which is a robust efficient and complete method for E/B-mode separation. We expect weak lensing to predominantly produce E-modes, making B-modes undesirable. Although the absence of B-modes does not guarantee a perfect data analysis, it is a necessary condition for a survey such as CFHTLenS. For future large-scale and space-based surveys, where the measurement errors are significantly smaller, the B-modes could also indicate other physical phenomena. For example, we know that some intrinsic alignment models predict these modes (see Blazek et al. 2011, and references therein). Before performing our analysis, we carried out a number of blind tests on cosmological simulations, to test the accuracy of our pipelines that are reported in the Appendix. The significance of the B-modes we found is highest for large scales, [40 arcmin, 100 arcmin], especially when the galaxies are divided into redshift bins. They also depend on the galaxy population used in the analysis. We repeated our analysis for blue and all galaxies, since blue galaxies do not show a strong intrinsic alignment signal.

Our COSEBIs measurement on tomographic data is the first of its kind. Previously, all COSEBIs data analysis has been limited to 2D cosmic shear data. Dividing galaxies into different redshift bins tightens the constraints on cosmological parameters, as it adds information about structure evolution, which is essential for constraining dark energy parameters. Adding redshift information to data analysis increases the total number of COSEBIs that need to be measured. This makes covariance matrix estimations more challenging, since a larger number of simulations are needed to reach a satisfactory precision. To alleviate this, we showed the first measurement of compressed COSEBIs (CCOSEBIs) that are composed of linear combinations of the COSEBIs that are most sensitive to cosmological information. This compression reduces the number of observables substantially. In this study, we used seven COSEBIs modes and six redshift bins. The total number of 147 COSEBIs

Table 4. Best-fitting values for $K_{\rm B}$, $K_{\rm E}^{\rm CFHTLenS}$, $K_{\rm E}^{\rm Planck}$, $K_{\rm B^c}$, $K_{\rm E^c}^{\rm CFHTLenS}$, $K_{\rm E^c}^{\rm Planck}$. We use a parameter, $K_{\rm X}$, to fit to the models given by $B_n = K_B$, $E_n = K_{\rm E}^{\rm CFHTLenS} E_n^{\rm CFHTLenS}$, $E_n = K_{\rm E}^{\rm Planck} E_n^{\rm Planck}$, $B^{\rm c} = K_{B^{\rm c}}$, $E^{\rm c} = K_{\rm E^c}^{\rm CFHTLenS} E^{\rm c,CFHTLenS}$ and $E^{\rm c} = K_{\rm E^c}^{\rm Planck} E^{\rm c,Planck}$. The errors on the fitted values show the $\Delta\chi^2 = 1$ value for the fit parameters. The CCOSEBIs values are only shown for the tomographic case where the number of CCOSEBIs modes is smaller than that of COSEBIs. The cases for which the p-values for null B-modes>0.01 are shown in boldface. The first column shows the angular range considered, while the following columns show the galaxies used, the number of redshift bins and the number of COSEBIs modes in the analysis.

				COSEBIs			CCOSEBIs		
θ range	Galaxies	z-bins	$n_{\rm max}$	$K_{\rm B} \times 10^{11}$	$K_{\rm E}^{\rm CFHTLenS}$	$K_{\rm E}^{\rm Planck}$	$K_{\rm B^c} \times 10^{15}$	$K_{\rm E^c}^{\rm CFHTLenS}$	$K_{\rm E^c}^{\rm Planck}$
$[1' - 100']$	All	1	2	**1.70 ± 1.39**	**1.32 ± 0.20**	**0.84 ± 0.13**	–	–	–
			7	**0.63 ± 1.29**	**1.41 ± 0.19**	**0.89 ± 0.12**	–	–	–
		6	2	1.80 ± 1.38	1.04 ± 0.17	0.68 ± 0.11	0.93 ± 13.36	1.08 ± 0.17	0.70 ± 0.11
			7	0.53 ± 1.26	1.06 ± 0.16	0.69 ± 0.10	26.13 ± 28.48	1.22 ± 0.16	0.79 ± 0.10
	Blue	1	2	**1.91 ± 1.60**	**1.38 ± 0.21**	**0.88 ± 0.13**	–	–	–
			7	**0.91 ± 1.50**	**1.41 ± 0.19**	**0.90 ± 0.12**	–	–	–
		6	2	1.23 ± 1.63	0.99 ± 0.17	0.65 ± 0.11	-6.64 ± 5.74	1.07 ± 0.17	0.70 ± 0.11
			7	0.65 ± 1.50	1.09 ± 0.16	0.71 ± 0.10	22.98 ± 18.93	1.15 ± 0.16	0.74 ± 0.10
$[1' - 40']$	All	1	2	**0.03 ± 0.65**	**1.45 ± 0.19**	**0.91 ± 0.12**	–	–	–
			7	**-0.48 ± 0.57**	**1.43 ± 0.19**	**0.90 ± 0.12**	–	–	–
		6	2	**-0.48 ± 0.65**	**1.15 ± 0.16**	**0.74 ± 0.10**	**-3.14 ± 2.87**	**1.16 ± 0.16**	**0.75 ± 0.10**
			7	**-0.63 ± 0.55**	**0.99 ± 0.16**	**0.64 ± 0.10**	**-2.44 ± 12.31**	**1.15 ± 0.16**	**0.75 ± 0.10**
	Blue	1	2	**-0.57 ± 0.78**	**1.53 ± 0.20**	**0.96 ± 0.13**	–	–	–
			7	**-1.34 ± 0.68**	**1.45 ± 0.20**	**0.92 ± 0.12**	–	–	–
		6	2	**-0.94 ± 0.77**	**1.18 ± 0.17**	**0.76 ± 0.11**	**0.46 ± 2.83**	**1.19 ± 0.17**	**0.77 ± 0.11**
			7	**-1.61 ± 0.67**	**1.00 ± 0.16**	**0.65 ± 0.10**	**15.47 ± 8.86**	**1.16 ± 0.17**	**0.75 ± 0.11**
$[40' - 100']$	All	1	2	-8.76 ± 3.36	3.12 ± 1.29	2.17 ± 0.90	–	–	–
			7	-2.25 ± 2.05	3.04 ± 1.27	2.12 ± 0.89	–	–	–
		6	2	-7.61 ± 3.38	3.39 ± 1.11	2.39 ± 0.79	-281.32 ± 316.00	2.74 ± 1.13	1.92 ± 0.81
			7	1.51 ± 1.99	2.68 ± 1.09	1.84 ± 0.77	-320.73 ± 557.68	3.17 ± 1.17	2.24 ± 0.83
	Blue	1	2	-9.79 ± 4.04	2.77 ± 1.45	1.94 ± 1.02	–	–	–
			7	-1.99 ± 2.44	2.57 ± 1.44	1.80 ± 1.01	–	–	–
		6	2	-8.05 ± 3.97	2.12 ± 1.20	1.52 ± 0.85	-222.44 ± 208.12	2.04 ± 1.20	1.47 ± 0.86
			7	1.91 ± 2.37	1.40 ± 1.21	0.98 ± 0.86	412.94 ± 508.33	1.81 ± 1.23	1.31 ± 0.88

modes were reduced to 20 CCOSEBIs to estimate 5 cosmological parameters. As a result, the estimated covariance for the CCOSEBIs has a higher precision.

We analysed our data according to angular scale and galaxy type, as well as analysing the data with and without tomographic redshift bins. We considered different samples of galaxies to compare our results with previous cosmic shear analyses of the CFHTLenS data. Since our analysis focuses on tests for systematic errors, instead of parameter estimation, we compare our measurements to two different flat ΛCDM cosmological models with *Planck* and CFHTLenS+*WMAP*7 best-fitting parameters. We calculated the goodness of fit of these two models to our data for the full range of analyses. The figure of merit used the p-value for a χ^2 analysis, which indicates the probability of finding a χ^2 value larger than the value found. We highlighted the values that corresponded to at least 99 per cent confidence. In addition, we used the same method to report the significance of the B-modes we found. We also used a simple parametrization to find the best-fitting values of a single parameter to our data. We find consistent results with Heymans et al. (2013), with little or insignificant B-modes in [1 arcmin, 40 arcmin] range. Both COSEBIs and CCOSEBIs show a better match to CFHTLenS cosmology over *Planck* for this angular range with redshift binning.

We compared our large-scale results with blue galaxies and tomography with Kitching et al. (2014), were we found the most significant B-mode signal, which is in tension with their finding of a zero B-mode. Our measured E-modes for this configuration show a slightly better match to *Planck* cosmology in agreement with Kitching et al. (2014). However, the cosmic shear information in this range is the lowest and as a result it has the weakest constraining power. On the other hand, as the modelling of baryons is associated with a rather large uncertainty, restricting the analysis to larger angular scales most likely removes systematics due to modelling.

Our results are in line with Kilbinger et al. (2013) who reported insignificant B-modes for a single redshift bin and a wide angular range with all galaxies. Our COSEBIs measurements in this range match with *Planck* cosmology better than CFHTLenS+*WMAP*7 that is also consistent with the parameter constraints from Kilbinger et al. (2013) that are in less tension with *Planck* than the tomographic CFHTLenS analysis.

Fu et al. (2014) have also reported B-modes in CFHTLenS for three-point statistics, using aperture mass statistics. Our results together show that there are remaining systematics left in the data. One hypothesis is that these systematics arise from selection effects that introduce a correlation between the PSF ellipticity and the galaxy ellipticity when galaxies are divided into redshift bins. The B-modes we measured are in general larger when tomography is considered. This will be investigated in more detail in our future work. Although not quantified here, we can see an anti-correlation between the E-modes and B-modes that is visible in the plots. This suggests that the systematic errors affect the E/B-modes in the same way.

The CCOSEBIs show insignificant B-modes for many cases that we have studied, even when the COSEBIs indicate otherwise. Currently, we do not have a full understanding of how systematic errors affect E/B-modes. This can be investigated by simulating systematic errors that show a similar signature to the ones found here, and examine their effect on E-modes. Nevertheless, assuming that the systematic errors affect the two modes in the same way (as

hinted by the E/B anti-correlation), we can conclude that for the cases where the CCOSEBIs B-modes are negligible, they are not degenerate with the cosmological parameters, which means that the B-modes detected by the COSEBIs should not bias the parameter estimations. Note that given the assumption above, if the CCOSEBIs modes are not sensitive to the systematics then they must be orthogonal to them.

The methods and pipelines used in this analysis can and should be used with any other reduced cosmic shear data set. COSEBIs is arguably the best method for testing for B-modes in the data and can also be used for measuring B-modes for cosmological analysis. Future and ongoing surveys will suffer more from inaccuracies in their covariance estimations, which can be remedied by either using a larger number of simulations or by decreasing the number of data points used in the analysis. As *N*-body simulations are expensive and time consuming we recommend using the compression method in Asgari & Schneider (2015) applied to COSEBIs to find CCOSEBIs and accurate cosmological parameters.

ACKNOWLEDGEMENTS

MA and CH acknowledge support from the European Research Council through grant number 240185 and 647112. MA acknowledges support from Scottish Universities Physics Alliance. CB acknowledges the support of the Australian Research Council through the award of a Future Fellowship. PS is supported by the Deutsche Forschungsgemeinschaft under the programme TR33 and SCHN-342/13. JHD acknowledges support from NSERC. Computations for the *N*-body simulations were performed on the GPC supercomputer at the SciNet HPC Consortium. SciNet is funded by the Canada Foundation for Innovation under the auspices of Compute Canada; the Government of Ontario; Ontario Research Fund – Research Excellence; and the University of Toronto. We thank the CFHTLenS team for making the data publicly available. This work is based on observations obtained with MegaPrime/MegaCam, a joint project of CFHT and CEA/IRFU, at the Canada–France–Hawaii Telescope (CFHT) that is operated by the National Research Council (NRC) of Canada, the Institut National des Sciences de l'Univers of the Centre National de la Recherche Scientifique (CNRS) of France, and the University of Hawaii. This research used the facilities of the Canadian Astronomy Data Centre operated by the National Research Council of Canada with the support of the Canadian Space Agency. CFHTLenS data processing was made possible thanks to significant computing support from the NSERC Research Tools and Instruments grant program.

REFERENCES

Addison G. E., Huang Y., Watts D. J., Bennett C. L., Halpern M., Hinshaw G., Weiland J. L., 2016, ApJ, 818, 132
Andrae R., Schulze-Hartung T., Melchior P., 2010, preprint (arXiv:1012.3754)
Asgari M., Schneider P., 2015, A&A, 578, A50
Asgari M., Schneider P., Simon P., 2012, A&A, 542, A122
Bartelmann M., Schneider P., 2001, Phys. Rep., 340, 291
Battye R. A., Moss A., 2014, Phys. Rev. Lett., 112, 051303
Becker M. R. et al., 2016, Phys. Rev. D, 94, 022002
Benjamin J. et al., 2013, MNRAS, 431, 1547
Blazek J., McQuinn M., Seljak U., 2011, J. Cosmol. Astropart. Phys., 5, 10
Bond J. R., Efstathiou G., 1984, ApJ, 285, L45
Choi A. et al., 2016, MNRAS, 463, 3737
Dossett J. N., Ishak M., Parkinson D., Davis T. M., 2015, Phys. Rev. D, 92, 023003
Eifler T., 2011, MNRAS, 418, 536
Erben T. et al., 2013, MNRAS, 433, 2545
Fu L., Kilbinger M., 2010, MNRAS, 401, 1264
Fu L. et al., 2014, MNRAS, 441, 2725
Harnois-Déraps J., van Waerbeke L., 2015, MNRAS, 450, 2857
Harnois-Déraps J., van Waerbeke L., Viola M., Heymans C., 2015, MNRAS, 450, 1212
Hartlap J., Simon P., Schneider P., 2007, A&A, 464, 399
Heymans C. et al., 2012, MNRAS, 427, 146
Heymans C. et al., 2013, MNRAS, 432, 2433
Hilbert S., Hartlap J., White S. D. M., Schneider P., 2009, A&A, 499, 31
Hildebrandt H. et al., 2012, MNRAS, 421, 2355
Huff E. M., Eifler T., Hirata C. M., Mandelbaum R., Schlegel D., Seljak U., 2014, MNRAS, 440, 1322
Joachimi B., Schneider P., 2008, A&A, 488, 829
Joudaki S. et al., 2016, preprint (arXiv:1601.05786)
Kilbinger M., 2015, Rep. Prog. Phys., 78, 086901
Kilbinger M. et al., 2013, MNRAS, 430, 2200
Kilbinger M., Bonnett C., Coupon J., 2014, Astrophysics Source Code Library, record ascl:1402.026
Kitching T. D. et al., 2014, MNRAS, 442, 1326
Köhlinger F., Viola M., Valkenburg W., Joachimi B., Hoekstra H., Kuijken K., 2016, MNRAS, 456, 1508
Kuijken K. et al., 2015, MNRAS, 454, 3500
Laureijs R. et al., 2011, preprint (arXiv:1110.3193)
MacCrann N., Zuntz J., Bridle S., Jain B., Becker M. R., 2015, MNRAS, 451, 2877
Mead A. J., Peacock J. A., Heymans C., Joudaki S., Heavens A. F., 2015, MNRAS, 454, 1958
Melchior P., Viola M., 2012, MNRAS, 424, 2757
Miller L. et al., 2013, MNRAS, 429, 2858
Planck Collaboration XIII, 2016a, A&A, 594, A13
Planck Collaboration XIV, 2016b, A&A, 594, A14
Press W. H., Teukolsky S. A., Vetterling W. T., Flannery B. P., 2002, Numerical Recipes in C++. Cambridge Univ. Press, Cambridge
Raveri M., 2015, preprint (arXiv:1510.00688)
Schneider P., Kilbinger M., 2007, A&A, 462, 841
Schneider P., van Waerbeke L., Jain B., Kruse G., 1998, MNRAS, 296, 873
Schneider P., van Waerbeke L., Mellier Y., 2002, A&A, 389, 729
Schneider P., Eifler T., Krause E., 2010, A&A, 520, A116
Sellentin E., Heavens A. F., 2016, MNRAS, 456, L132
Semboloni E., Hoekstra H., Schaye J., van Daalen M. P., McCarthy I. G., 2011, MNRAS, 417, 2020
Semboloni E., Hoekstra H., Schaye J., 2013, MNRAS, 434, 148
Simpson F. et al., 2013, MNRAS, 429, 2249
Smith R. E. et al., 2003, MNRAS, 341, 1311
Spergel D. N., Flauger R., Hložek R., 2015, Phys. Rev. D, 91, 023518
Takahashi R., Sato M., Nishimichi T., Taruya A., Oguri M., 2012, ApJ, 761, 152
Taylor A., Joachimi B., 2014, MNRAS, 442, 2728
The Dark Energy Survey Collaboration et al., 2015, preprint (arXiv:1507.05552)
Velander M. et al., 2014, MNRAS, 437, 2111
Verde L., Feeney S. M., Mortlock D. J., Peiris H. V., 2013, J. Cosmol. Astropart. Phys., 9, 13

APPENDIX A: PIPELINE OPTIMIZATION AND VERIFICATION

In this appendix, we present a series of tests to explore the effects of noise and discrete integration on the determination of the COSEBIs for CFHTLenS-like data.

A1 Power spectra versus 2PCFs

In Asgari et al. (2012), we calculated COSEBIs numerically, assuming a perfect knowledge, i.e. a noise-free measurement, of the

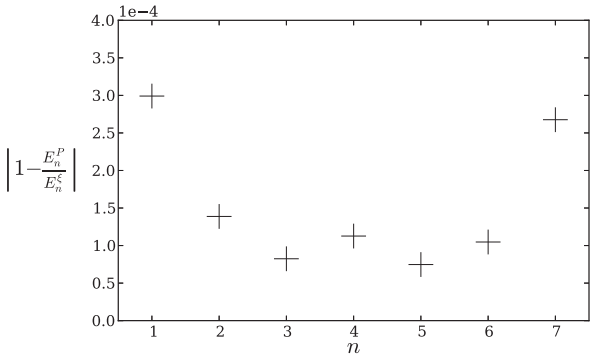

Figure A1. A comparison between two methods of finding E-COSEBIs. E_n^P is calculated from equation (6), while E_n^ξ estimated from equation (4). E_n with $n = 1$–7 are shown here for an angular range of [1 arcmin, 400 arcmin].

input quantities. We used equation (6) to find the E-mode COSEBIs that is more convenient to use for a theoretical analysis, since most theories provide us with an input power spectrum. However, in practice shear 2PCFs are more straightforward to measure, from which COSEBIs can then be inferred via equation (4). The first test therefore checks if equations (6) and (4) result in the same E_n when calculated numerically assuming noise-free data. For this test, we choose an angular range of [1 arcmin, 400 arcmin]. Fig. A1 shows the residual ratio of E_n numerically calculated from equations (6) and (4) for $n = 1$–7. As we can see in this figure, the values of E_n from the two methods agree to better than 0.03 per cent. Fig. 10 of Asgari et al. (2012) shows the dependence of three cosmological parameters to the first five COSEBIs. From this figure, we conclude that the small difference between E_n from equations (6) and (4) is therefore indeed insignificant for our analysis (for example, if σ_8 changes by 1 per cent then E_1 will change by about 2 per cent).

A2 From smooth integration to noisy trapezoidal

In Appendix A1, we assumed a perfect knowledge of the 2PCFs over the angular range considered, a Gaussian integration method (see Press et al. 2002) between two extrema of the integrand is employed to evaluate E_n in both cases. In practice, however, we only have the values of 2PCFs in angular bins or at certain θ values. Consequently, we need to use a different integration routine to evaluate E_n from equation (4) for real data. The most straightforward integration method is the trapezoidal method for a linearly binned data. In this section, we determine how many linear angular bins are needed to reach a certain accuracy in determining E_n.

The solid curves in Fig. A2 show the fractional deviation of E_n as a function of angular bins used in the trapezoidal integration assuming noise-free data. All the E_n values are normalized by their true value, calculated from the convergence power spectrum using equation (6). As can be seen in Fig. A2, a larger number of angular bins are required for the higher COSEBIs modes, to reach the same accuracy. The reason for this behaviour is that the $T_{\pm n}(\vartheta)$ functions have $n + 1$ roots in their range of support and oscillate around them. Consequently, the higher modes are more sensitive to the number of θ bins incorporated in their integral (see Schneider et al. 2010; Asgari et al. 2012). Following fig. 10 in Asgari et al. (2012) we choose an accuracy of 0.5 per cent for E_n that corresponds to an accuracy on σ_8 of 0.25 per cent. This enforces a lower limit of 10 000 bins for, E_7, the highest COSEBIs mode we use in this analysis.

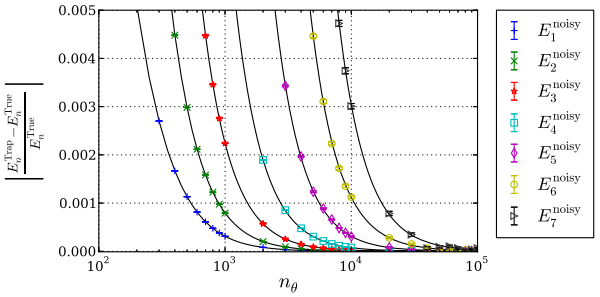

Figure A2. The effect of noise on the estimated E_n for the first seven modes. Here, we only consider uncorrelated noise between the angular bins. n_θ is the number of angular bins for the 2PCFs. The error bars are calculated from the variance between the noise realizations. The black solid curves show the E_n values without any added noise.

We next include the effects of noise on the estimated E_n. Since the number of bins needed to reach the accuracy desired is high, the shot noise term of the correlation function covariance dominates the other terms in this case. We will therefore choose to ignore other sources of noise for this test, using only the shot noise in the covariance, at this stage. We can make a noisy $\xi_\pm(\theta)$ mock data set from

$$\xi_\pm(\theta)^{\rm Noisy} = \xi_\pm(\theta) + N \times R, \tag{A1}$$

where

$$N = \sqrt{\frac{\sigma_\epsilon^4}{4\pi A \bar{n}^2 \Delta\theta\, \theta}}, \tag{A2}$$

is the square root of the shot noise term in the 2PCFs covariance (see Joachimi & Schneider 2008, for example), with $\sigma_\epsilon = 0.279$, the intrinsic ellipticity dispersion of the galaxies, $A = 154$ deg^2, the area of the survey, $\bar{n} = 11$ arcmin^2, the effective mean number density of galaxies and $\Delta\theta$ the width of the angular bins. R is a randomly generated number from a Gaussian distribution with a variance of 1 and a mean of 0. With the above definitions the covariance of $\xi_\pm(\theta)^{\rm Noisy}$ is equal to the desired covariance. The symbols in Fig. A2 show the ensemble average estimate of E_n from 50 $\xi_\pm(\theta)^{\rm Noisy}$ realizations with respect to the number of angular bins. The errors shown are the standard deviation of the mean value of E_n over all the realizations. The presence of the random errors do not change the conclusions drawn from the previous test. By comparing the curves and the symbols in Fig. A2, we can also conclude that the random noise due to the intrinsic ellipticity dispersion of galaxies does not bias the estimation of COSEBIs.

A3 Simulations: covariance matrix estimation

In this section we determine COSEBIs on the mock data from the SLICS simulations that resemble the CFHTLenS data. Here, we also show the covariance matrices that are used in the main analysis and are estimated from the simulated data. In this paper, we use the second version of the CFHTLenS CLONE catalogue,[7] which is based on the SLICS N-body simulations (see Harnois-Déraps & van Waerbeke 2015, for details) and consist of 497 independent lines of sight, 60 deg^2 each. These mock catalogues are specifically made for the CFHTLenS data, taking into account its redshift

[7] The first version is available on www.cfhtlens.org.

distribution. Furthermore, source clustering effects are included in these catalogues. The limited box size of the simulations dictates the maximum scale that can be trusted. In addition, the resolution of the simulations put limits on the small scales. Combining this with the fact that on small scales, baryonic effects (not included in the simulations) become important, we limit our minimum angular range as well (see Semboloni et al. 2011, for the effects different baryon feedback models have on structure formation and $\xi_{\pm}$). Hence, we choose to only use scales in [1 arcmin, 100 arcmin] in our analysis.

Since the simulated covariance is different from the Gaussian random noise we used in Appendix A2, we repeat the angular bin versus measured E_n test using the simulated data. The covariance of the COSEBIs is defined as

$$\mathbf{C}_{mn} \equiv \langle E_m E_n \rangle - \langle E_m \rangle \langle E_n \rangle, \tag{A3}$$

where $\langle E_n \rangle$ is the expectation value of E_n. The covariance is estimated from the simulations via,

$$\mathbf{C}_{mn} = \frac{1}{N-1} \sum_{i=1}^{N} \left(E_m^i - \langle E_m \rangle \right) \left(E_n^i - \langle E_n \rangle \right), \tag{A4}$$

where

$$\langle E_n \rangle = \frac{1}{N} \sum_{i=1}^{N} E_n^i, \tag{A5}$$

is the mean E_n over all lines of sight of the $N = 497$ simulated fields.

We find similar conclusions from repeating the bin size exercise. Nevertheless, for the rest of the analysis we choose to use 4×10^5 linear bins in [1 arcmin, 100 arcmin], which is larger than the threshold we found in the previous section. With a narrower angular binning scheme the number of galaxies in each bin decreases. Hence the $\xi_{\pm}$ estimate is noisier. In this analysis, we ensured that all the bins are populated with galaxies. Increasing the number of 2PCFs angular bins cannot reduce the accuracy of the estimated COSEBIs, as long as all the angular bins are populated with pairs of galaxies.

The COSEBIs covariance for a single redshift distribution from the simulations is shown in Fig. A3, for the three angular ranges [1 arcmin, 100 arcmin], [1 arcmin, 40 arcmin] and [40 arcmin, 100 arcmin]. The right-hand panels show the covariance for E_n while the left-hand panels show the same for B_n. All the covariances are scaled by a factor of $60 \times 497/94.564$ to correspond to the effective CFHTLenS area, where we have 497 mock fields, 60 deg^2 each. The effective area of CFHTLenS passed fields is 94.564 deg^2.

In the simulated catalogues a mock best-fitting value of each galaxy's redshift, $z_{\rm B}$, is given, which is in general different from its spectroscopic value. To mimic the real data, we use $z_{\rm B}$ to choose which redshift bin a galaxy belongs to. While tomographic bins have no overlap in $z_{\rm B}$, this is not the case for the underlying true redshift distribution.

Fig. A4 shows the covariance matrices for [1 arcmin, 100 arcmin] with the six redshift bins in Table 1. Each block in the covariance matrix has 7^2 elements corresponding to a combination of redshift bin pairs. The *x*/*y*-axis in the plots show the redshift bin pairs considered. In total, the covariance has 147^2 elements. The left- and right-hand panels show the covariance matrix for the E_n and B_n, respectively. In Fig. A4, we see that for all cases, the value of the covariance drops for the off-diagonal elements. Although not shown here for the tomographic case, for both redshift binning cases the [40 arcmin, 100 arcmin] range has a more diagonal covariance. This is due to the fact that non-Gaussian effects are less important for this angular range. Therefore, any analysis that only uses this angular range is less likely to be biased because of poor modelling of non-linear scales. However, the cosmic shear information in this angular range is significantly lower than that of the lower angular scales.

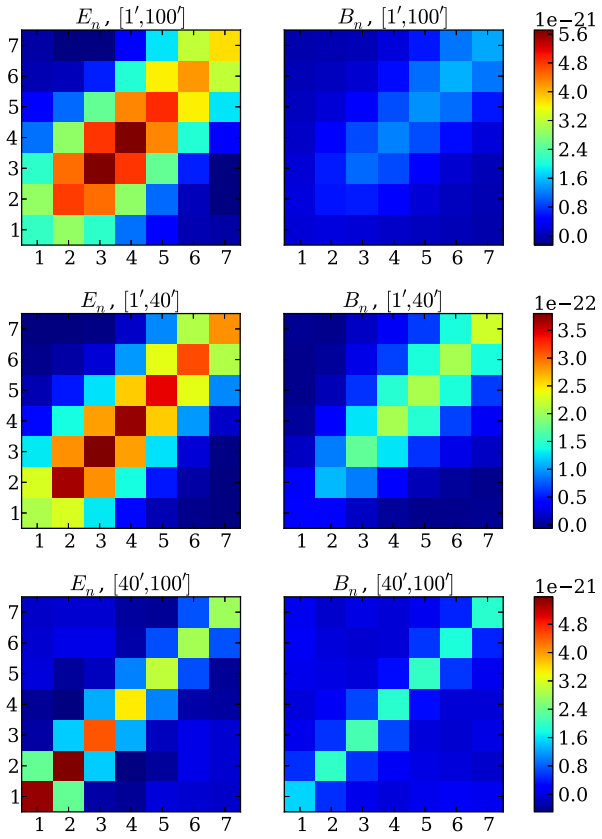

Figure A3. Covariance matrices of COSEBIs for a single redshift distribution. Three angular ranges, [1 arcmin, 100 arcmin], [1 arcmin, 40 arcmin] and [40 arcmin, 100 arcmin] are considered here. The *x*/*y*-axis show the COSEBIs mode considered. The COSEBIs are less correlated for [40 arcmin, 100 arcmin] compared to the other cases.

Fig. A5 shows the covariance matrices for the E-mode and B-mode CCOSEBIs for six redshift bins and $\theta \in$ [1 arcmin, 100 arcmin], measured from the SLICS simulations. The *x*-/*y*-axis show the CCOSEBIs modes for which the covariance is shown. In this work, we chose five cosmological parameters, σ_8, $\Omega_{\rm m}$, n_s, h and $\Omega_{\rm b}$. This means that we have 5 first-order CCOSEBIs that depend on the covariance and the first-order derivatives of the COSEBIs with respect to the parameters, and 15 second-order CCOSEBIs that depend on the covariance and the second-order derivatives of the COSEBIs with respect to the parameters. Hence, we show the CCOSEBIs modes by the parameters with respect to which the compression is made. In total, for 5 parameters, there are 20 CCOSEBIs modes irrespective of the number of redshift bins. Hence, for the case of 6 redshift bins, we have compressed 147 parameters to only 20 and reduced the size of the covariance substantially, as can be seen by comparing Figs A4 and A5. The cross-covariance between the CCOSEBIs modes is relatively high for some of the cases. This is due to the fact that the CCOSEBIs modes are based on cosmological parameters that can have large degeneracies. For example, the $\Omega_{\rm m}$ and σ_8 that have a large degeneracy in cosmic shear analysis, also show a large cross-covariance.

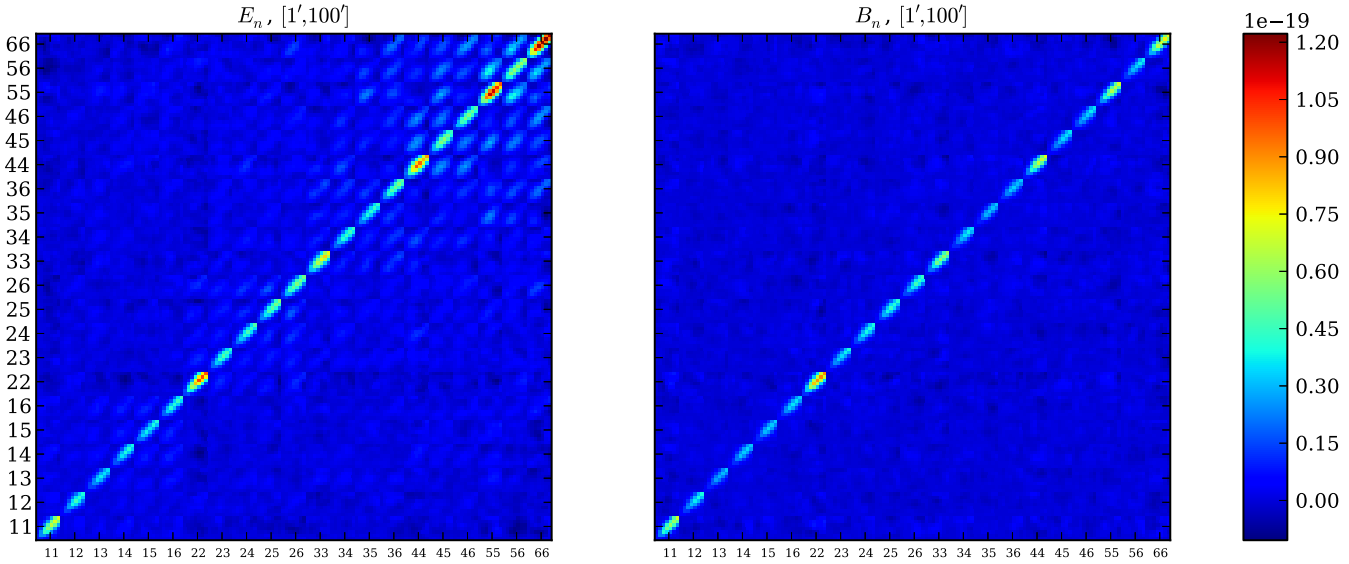

Figure A4. Covariance matrices of COSEBIs for six redshift bins. Three angular ranges, [1 arcmin, 100 arcmin], [1 arcmin, 40 arcmin] and [40 arcmin, 100 arcmin] are considered here. The *x*/*y*-axis show the redshift bin combination, for example '13' means redshift bins 1 and 3 are relevant. There are seven COSEBIs modes for each combination.

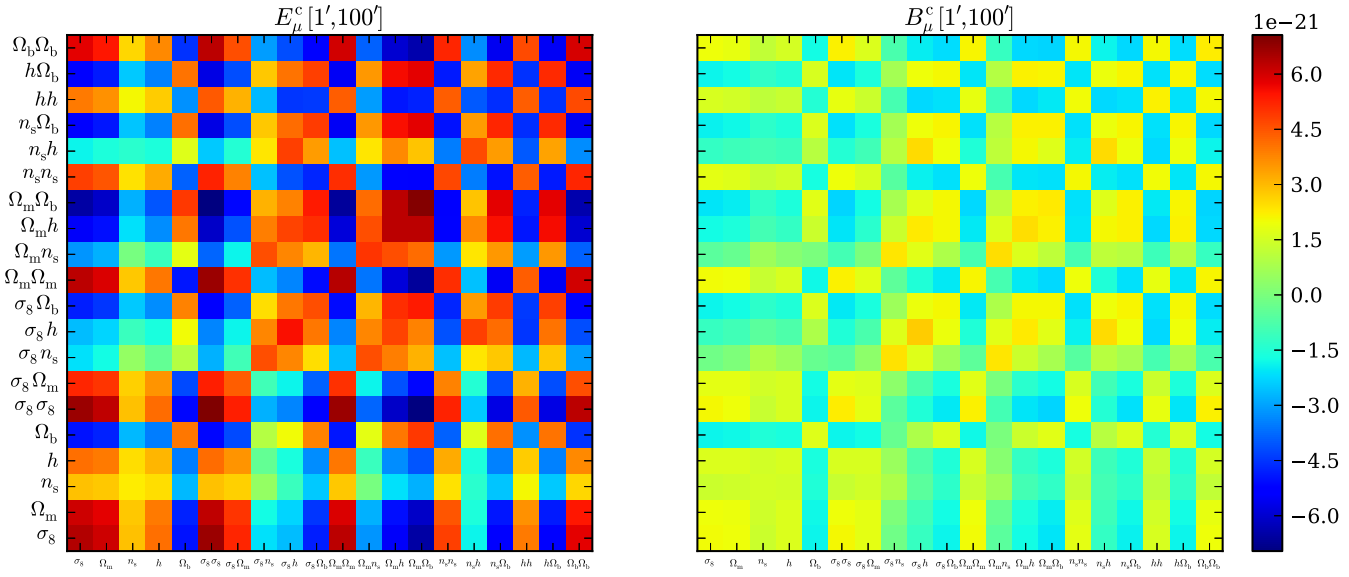

Figure A5. Covariance matrices of CCOSEBIs for six redshift bins estimated from SLICS simulations. The angular range [1 arcmin, 100 arcmin] is considered here. The left- and right-hand panels show the covariances for the E-modes and B-modes, respectively. The CCOSEBIs are linear combinations of COSEBIs. The CCOSEBIs modes are denoted by the parameter(s) that they are most sensitive to. A comparison of the number of elements in the COSEBIs covariance for six redshift bins in Fig. A4 and this figure shows the significance of this compression method.

A4 B- and E-mode analysis of mocks

The simulated mock catalogues should be B-mode free, providing an opportunity to explore how random ellipticity noise can affect the measured B-modes. For each line of sight, we measure all B_n values and determine the χ^2 values for $B_n = 0$,

$$\chi^2_B = \boldsymbol{B}^{\rm t}\mathbf{C}^{-1}\boldsymbol{B}, \tag{A6}$$

where $\boldsymbol{B}$ is the vector and $\mathbf{C}$ is the covariance matrix of B_n. Fig. A6 shows the distribution of the χ^2_B for the 497 SLICS simulations (green histograms). The left-hand panel belong to the single redshift case, whereas the tomographic case is shown in the right-hand panel. Since, in this study, we used 7 COSEBIs modes the degrees of freedom for the single redshift bin case is 7, while for the tomographic case it is 147. The blue solid curves show the theoretical χ^2 distribution for a given degrees of freedom, and they match the histograms.[8] Consequently, we conclude that the B-modes in the simulations are statistically consistent with zero and provide a χ^2 distribution with which to compare the real data. The red arrows show the value of the B-modes χ^2 corresponding to the CFHTLenS data with $\theta \in$ [1 arcmin, 100 arcmin]. We can see that the blue galaxies show a more significant B-mode signal compared to all galaxies. Furthermore, the χ^2 values of the CFHTLenS data for the tomographic case are well beyond what is expected from the simulations. We also calculated the CCOSEBIs from the simulations

[8] We checked this using a Kolmogorov—Smirnov test.

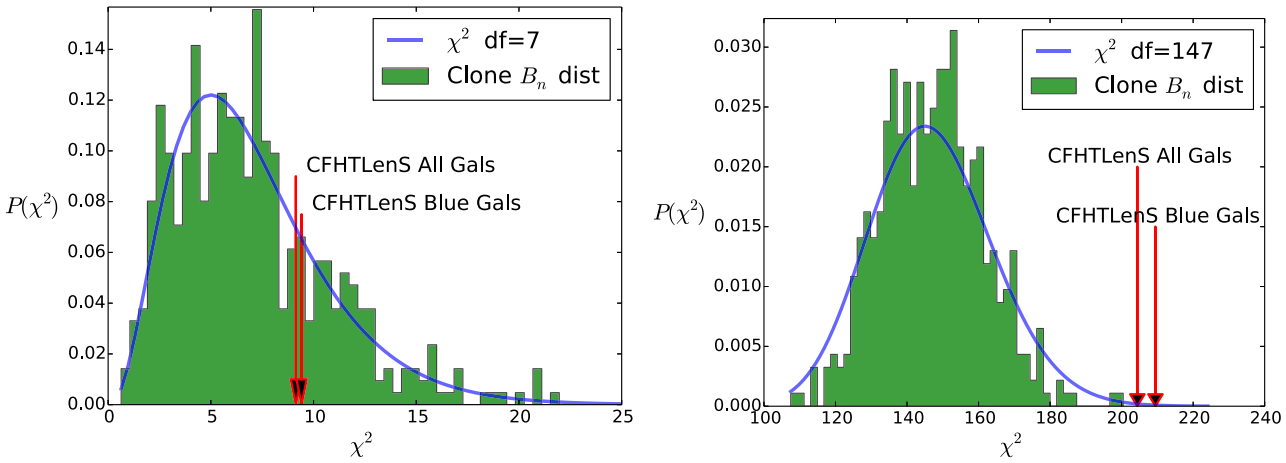

Figure A6. χ^2 distribution of B_n assuming a zero B-modes model for the Clone simulations (green histogram). The left plot corresponds to a single redshift distribution with 7 B_n modes, while the right corresponds to 6 redshift bins with 7 B_n modes resulting in 147 modes in total. The blue curves show the theoretical χ^2 distribution with the given degrees-of-freedom, df. The arrows show the χ^2 values for the B-modes in [1 arcmin, 100 arcmin] range in the CFHTLenS data for the corresponding cases.

and confirmed that they follow a χ^2 distribution with 20 degrees of freedom.

The E-mode COSEBIs were also optimized and tested using the same set of catalogues. We performed a blind analysis of the mocks to test if the input cosmology of the simulations can be recovered. The χ^2 distributions for the $E_n - E_n^{\rm th}$, where E_n is estimated from the simulations and $E_n^{\rm th}$ is its expected theory value, are very similar to the χ^2 distributions of the B_n (Fig. A6), hence we do not show them here. The CFHTLenS data analysis was then carried out without any changes to the pipelines.

APPENDIX B: χ^2 VALUES AND DEGREES OF FREEDOM

Comparing raw χ^2 values can be misleading for two reasons: first, a χ^2 distribution is asymmetric and secondly, this distribution highly depends on the degrees of freedom associated with the χ^2 value. However, in Table B1, we provide the degrees of freedom for each element in Table 3 and the χ^2 values to give the readers the opportunity to perform their own interpretation of the data.

Table B1. The number of degrees of freedom of the χ^2 value for each entry in Table 3.

θ range	Galaxies	z-bins	$n_{\max}$	COSEBIs						CCOSEBIs					
				B_n		$E_n^{\rm CFHTLenS}$		$E_n^{\rm Planck}$		$B^{\rm c}$		$E^{\rm c,\ CFHTLenS}$		$E^{\rm c,\ Planck}$	
				DOF	χ^2	DOF	χ^2	DOF	χ^2	DOF	χ^2	DOF	χ^2	DOF	χ^2
[1 arcmin − 100 arcmin]	All	1	2	2	1.60	2	3.67	2	2.15	–	–	–	–	–	–
			7	7	9.29	7	14.71	7	9.73	–	–	–	–	–	–
		6	2	42	82.85	42	80.16	42	90.06	20	34.70	20	31.05	20	39.37
			7	147	291.33	147	322.10	147	335.59	20	15.32	20	51.11	20	53.41
	Blue	1	2	2	3.11	2	5.43	2	2.10	–	–	–	–	–	–
			7	7	9.57	7	23.20	7	18.24	–	–	–	–	–	–
		6	2	42	90.28	42	66.91	42	77.73	20	32.31	20	24.55	20	31.77
			7	147	298.54	147	285.77	147	295.41	20	20.67	20	29.42	20	34.65
[1 arcmin − 40 arcmin]	All	1	2	2	0.60	2	6.97	2	1.36	–	–	–	–	–	–
			7	7	4.43	7	11.79	7	6.41	–	–	–	–	–	–
		6	2	42	66.64	42	80.64	42	85.12	20	24.98	20	35.09	20	39.45
			7	147	275.17	147	290.76	147	307.95	20	18.21	20	43.23	20	47.66
	Blue	1	2	2	0.86	2	8.17	2	0.26	–	–	–	–	–	–
			7	7	8.88	7	22.03	7	16.46	–	–	–	–	–	–
		6	2	42	66.43	42	69.16	42	72.39	20	16.93	20	23.36	20	26.25
			7	147	226.22	147	287.05	147	304.01	20	31.20	20	28.35	20	32.54
[40 arcmin − 100 arcmin]	All	1	2	2	11.01	2	6.47	2	5.40	–	–	–	–	–	–
			7	7	22.79	7	13.74	7	12.68	–	–	–	–	–	–
		6	2	42	85.72	42	73.14	42	71.48	20	33.30	20	42.92	20	41.92
			7	147	387.35	147	376.98	147	375.72	20	34.68	20	41.61	20	40.31
	Blue	1	2	2	10.54	2	3.79	2	3.10	–	–	–	–	–	–
			7	7	22.29	7	14.72	7	14.11	–	–	–	–	–	–
		6	2	42	79.81	42	62.68	42	62.03	20	49.61	20	29.42	20	28.83
			7	147	391.02	147	341.97	147	341.87	20	48.61	20	27.27	20	26.84

This paper has been typeset from a TEX/LATEX file prepared by the author.